JACS
JOURNAL OF THE AMERICAN CHEMICAL SOCIETY
Article
pubs.acs.org/JACS

Indium-Based Ultraviolet-Transparent Electroconductive Oxyfluoride InOF: Ambient-Pressure Synthesis and Unique Electronic Properties in Comparison with In_2O_3

Tatsuya Mori,[†] Koichi Kajihara,*[,†] Kiyoshi Kanamura,[†] Yoshitake Toda,[‡] Hidenori Hiramatsu,[‡] and Hideo Hosono[‡]

[†]Department of Applied Chemistry, Graduate School of Urban Environmental Sciences, Tokyo Metropolitan University, 1-1 Minami-Osawa, Hachioji 192-0397, Japan

[‡]Materials and Structures Laboratory & Frontier Research Center, Tokyo Institute of Technology, 4259 Nagatsuta, Midori-ku, Yokohama 226-8503, Japan

ABSTRACT: A method for the synthesis of single-phase powdered InOF under ambient pressure has been developed. The method involves pyrolysis of a hydrate of InF_3 in an O_2 atmosphere of controlled humidity. Various intermediate phases were formed during the pyrolysis, and their structures and interconversions were analyzed. Combined results of optical absorption measurements and density functional calculations indicate that InOF is a direct band gap material with a band gap energy of ~3.7 eV. Unlike In_2O_3, the electrical conductivity of polycrystalline InOF pellets can be controlled over ~8 orders of magnitude from ~10^{-8} S cm^{-1} to ~2 S cm^{-1} by thermal annealing, and the sample with the highest conductivity was a nearly degenerate n-type semiconductor with a relatively small carrier concentration of ~10^{18} cm^{-3}. The work function of InOF measured by ultraviolet photoelectron spectroscopy is ~3.5 eV and is smaller by ~1.5 eV than that of In_2O_3. This difference comes from a decrease in the electron affinity.

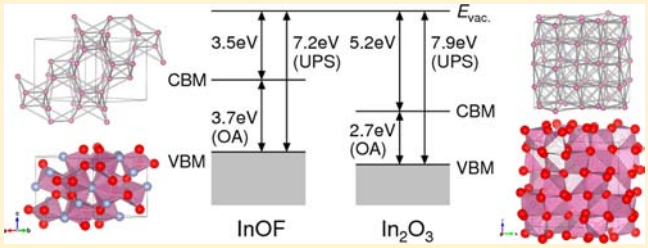

INTRODUCTION

Optical and electrical materials that are transparent to ultraviolet (UV) light have attracted attention because of the recent development of UV lasers and light-emitting diodes and their increased use in sensing, sanitization, lighting, and processing. Oxides are an important class of materials for such applications. However, their band gap energies are often not large enough to transmit UV light, because of the relatively high energy of the valence band, which consists mainly of 2p orbitals of O^{2-} ions. The band gap energies of fluorides are generally larger than those of oxides containing the same metallic elements, because the energy of the 2p orbitals of F^- ions is deeper than that of O^{2-} ions. Fluorides and oxyfluorides may therefore be promising as candidates for UV-transparent electrically conductive ceramics. Doping or treatments of transparent conductive oxides with fluorine are also useful in increasing the carrier concentrations, decreasing the refractive indices, and modifying the work functions, which is a key parameter to device applications.

Indium oxide and its derivatives are the most important conductive oxides transparent to visible light, and their UV transparency may be improved by the incorporation of fluorine. Fluorine doping of amorphous In_2O_3 has been examined, and a small increase in the band gap energy was observed, along with an increase in the carrier concentration and a decrease in the refractive index.[1] InOF is a crystalline compound known in the In−O−F ternary system.[2−5] It is an anion-ordered oxyfluoride belonging to the orthorhombic crystal system (space group no. 70, *Fddd*) and consists of distorted InO_4F_2 octahedra bridged by the O−O edges and the corner F atoms.[5] InOF is prepared by the fluorination of InOI or InOCl.[2] The crystal structure and electrical properties of InOF have been studied using single crystalline samples synthesized by direct reaction between InF_3 and In_2O_3 in an evacuated Pt tube or a high-pressure cell between 800 °C and 1000 °C.[4,5] The resultant single crystalline samples exhibit a metallic conductivity of ~10^2 S cm^{-1}.[4] Another method of forming InOF is the pyrolysis of $InF_3{\cdot}3H_2O$ at ambient pressure.[3] In contrast to anhydrous InF_3, which is highly hygroscopic, $InF_3{\cdot}3H_2O$ is stable and suitable as a starting material. However, its simple pyrolysis in air is accompanied by the formation of impurity phases, including In_2O_3, and it does not give single-phase InOF.[3] Because of these synthetic difficulties, InOF has received little attention, and the optical and electrical properties are largely unknown.

In this paper, we report the synthesis of single-phase InOF at ambient pressure by pyrolysis of $InF_3{\cdot}3H_2O$ in a controlled atmosphere and the optical and electrical properties including the electronic band structure. It turns out that the electrical conductivity of InOF can be varied from a substantially nonconductive state to a good conductive state. The work function of InOF is smaller by ~1.5 eV than that of In_2O_3. This

Received: June 12, 2013
Published: August 21, 2013

   dx.doi.org/10.1021/ja405889m | *J. Am. Chem. Soc.* 2013, 135, 13080−13088

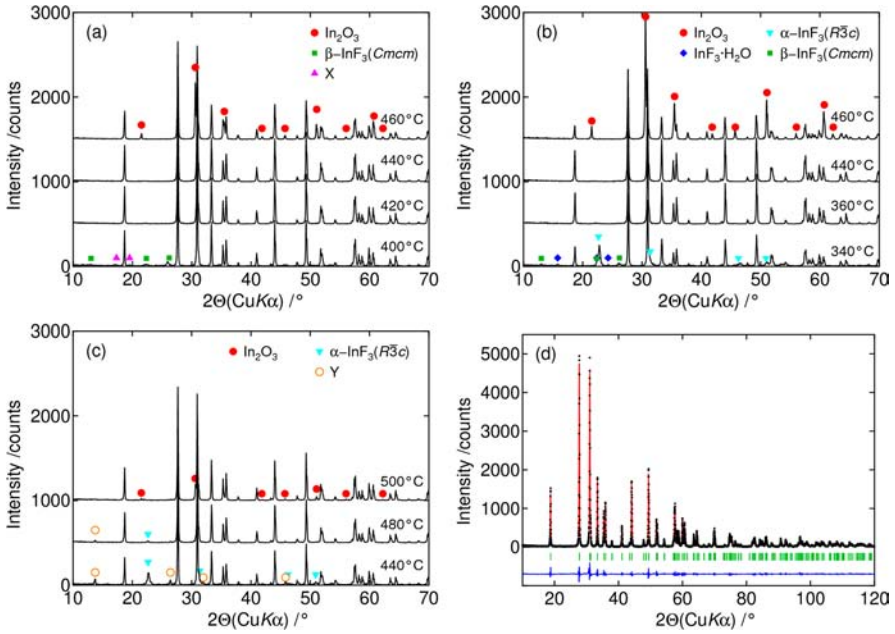

Figure 1. XRD patterns of powdered samples prepared by pyrolysis of 0.5 g of $InF_3·3H_2O$ at various temperatures with (a) dry N_2 or (b) dry O_2 purging prior to heating, and (c) a flow of dry O_2 during heating. Diffraction peaks from InOF are not marked. (d) XRD pattern and Rietveld analysis of a powdered sample prepared from 3.0 g of $InF_3·3H_2O$ with a flow of humidified (wet) O_2 below ~300 °C and dry O_2 above the temperature.

finding is explained by a high energy shift of the conduction band minimum arising from fewer nearest In−In neighbors and the resultant narrowing of the conduction band.

■ EXPERIMENTAL PROCEDURES

Polycrystalline samples of InOF were synthesized by the thermal decomposition of $InF_3·3H_2O$ (Kojundo Chemical Laboratory) in a tube furnace (1000 mm × 42 mm ϕ in volume, with a soaking zone length of ~50 mm). Sn-added samples were prepared by mixing $InF_3·3H_2O$ and $(NH_4)_2SnF_6$ (Aldrich) at an In:Sn atomic ratio of 0.95:0.05. The precursor was heated at 200 °C h^{-1} and maintained for 0.5 h at the target temperature, unless otherwise stated. The resultant powder was then pressed at 50 MPa and sintered for 2 h at the target temperature after heating at 200 °C h^{-1} with flowing N_2, O_2, or H_2 at 20 mL min^{-1} throughout the heating program. The samples were characterized using X-ray diffraction (XRD, RINT Ultima II, Rigaku), and the structure parameters were refined by the Rietveld method using RIETAN-FP.[6] Infrared (IR) absorption spectra of powdered samples were measured using a Fourier transform IR spectrometer (FT/IR-6300, JASCO) and the KBr pellet method. Diffuse reflectance spectra were measured using a conventional spectrometer (U-4100, Hitachi). The electrical transport properties were evaluated by Hall effect measurements using the van der Pauw configuration under ac modulation of a magnetic field (model RESISTEST 8300, Toyo). X-ray photoelectron spectroscopy (XPS) and ultraviolet photoelectron spectroscopy (UPS) measurements were performed using a hemispherical analyzer (Omicron) with nonmonochromatic UV (He I line, $h\nu$ = 21.2 eV, ΔE = 0.1 eV) and X-ray (Al $K\alpha$ line, $h\nu$ = 1486.6 eV, ΔE = 1.0 eV) sources, respectively. Samples were placed in an ultrahigh vacuum apparatus with a base pressure of 2×10^{-8} Pa and cleaned by 1 keV Ar^+ ion sputtering. The energy scale of XPS spectra was calibrated to the Au $^4f_{7/2}$ peak at 84.0 eV. The electronic structure was calculated via the full-potential linearized augmented plane wave/augmented plane wave + local orbitals (LAPW/APW+lo) method using WIEN2k with PBE96 GGA functionals.[7] The cutoff energy for the plane wave was 167 eV.

■ RESULTS

Synthesis of Single-Phase InOF. The pyrolysis of $InF_3·3H_2O$ was examined under various conditions. Figures 1a,b shows XRD patterns of powdered samples synthesized by pyrolyzing 0.5 g of $InF_3·3H_2O$ after purging the furnace with dry N_2 or O_2, without a gas flow during the heat treatment ("purge" experiment). Single-phase InOF was obtained at temperatures between 420 °C and 440 °C in N_2, and between 360 °C and 440 °C in O_2. In both cases, In_2O_3 was formed at or above 460 °C. In contrast, single-phase InOF was obtained at much lower temperatures in O_2 than in N_2. The main impurity phases remaining below the threshold temperature were α-InF_3,[8] β-InF_3,[9] $InF_3·3H_2O$,[10] and an unidentified phase, X. An increase in the initial amount of $InF_3·3H_2O$ slowed the oxidation of the fluorides at lower temperatures and narrowed the temperature range for the formation of single-phase InOF. In the O_2 purge experiment, the low-temperature threshold for the formation of single-phase InOF from 1.0 g of $InF_3·3H_2O$ was 440 °C. The main impurity phase remaining below the temperature was α-InF_3.

Figure 1c shows XRD patterns of samples synthesized with dry O_2 flowing at 100 mL min^{-1} during the pyrolysis of 0.5 g of $InF_3·3H_2O$. The gas flow raised the temperature of formation of In_2O_3. However, the low-temperature threshold for the disappearance of impurity phases was raised, along with the appearance of another unknown phase, Y, making it difficult to obtain single-phase InOF.

The pyrolysis was also conducted with dry O_2 flowing at 100 mL min^{-1} with humidification below ~300 °C, by simply bubbling O_2 through distilled water at room temperature. This procedure was found to be effective in increasing the amount of InOF obtained. Figure 1d shows the XRD pattern and Rietveld analysis of the sample prepared by pyrolyzing 3.0 g of $InF_3·3H_2O$ for 2 h at 440 °C. The good agreement between the observed and simulated patterns confirmed the formation of single-phase InOF. The refined structure parameters, listed in

dx.doi.org/10.1021/ja405889m | J. Am. Chem. Soc. 2013, 135, 13080−13088

Table 1, also agree well with those determined by single-crystal XRD analysis.[5] The resultant InOF powder was stable in an ambient atmosphere and in toluene but decomposed in water within a few hours.

Table 1. Results of Rietveld Analysis of XRD Pattern Shown in Figure 1d[a]

atom	site	occup.	x	y	z	U (Å^2)
In	16f	1	0.32602(7)	1/8	1/8	0.0040(2)
O	16g	1	1/8	0.2612(5)	1/8	0.008(14)
F	16d	1	1/2	1/2	1/2	0.018(15)

[a] R-values: R_{wp} = 12.28%, R_I = 1.63%, R_F = 1.15%, S = 1.20. Phase: InOF. Space group *Fddd* (no. 70), Z = 16. Lattice parameters: a = 8.347(17) Å, b = 10.177(2) Å, c = 7.031(15) Å.

An Sn-added InOF powdered sample was prepared by pyrolyzing 1.0 g of $InF_3{\cdot}3H_2O$ containing $(NH_4)_2SnF_6$ for 2 h at 440 °C under an N_2-purged condition. The XRD pattern (not shown) was essentially identical to that of single-phase InOF. The lattice parameters were a = 8.345(3) Å, b = 10.178(3) Å, and c = 7.032(2) Å and were similar to those of undoped InOF (Table 1). Thus, the substitution of Sn into the lattice of InOF was not obvious.

Observations of Intermediate Phases. To examine the details of the conversion of $InF_3{\cdot}3H_2O$ into InOF, the crystalline phases formed during pyrolysis were investigated. Figure 2a shows XRD patterns of samples treated at 200 °C and 300 °C in O_2 or N_2 purge experiments and at 320 °C in O_2 flow experiments. The samples subjected to the O_2 flow experiments were not retained at the target temperature. In all samples, β-InF_3 was observed as the main crystalline phase. The presence of $InF_3{\cdot}3H_2O$ and the unknown phase X was also confirmed. In addition, a crystalline phase, which can be indexed to α-InF_3 with lattice parameters slightly different from the normal values, was found. The amounts of $InF_3{\cdot}3H_2O$ and the unknown phase X were smallest in the sample treated at 320 °C in the wet O_2 flow experiment, and the Rietveld analysis results are shown in Figure 2b. A two-phase model of β-InF_3 and α-InF_3 gave a good fit, and the refined structure parameters are listed in Table 2.

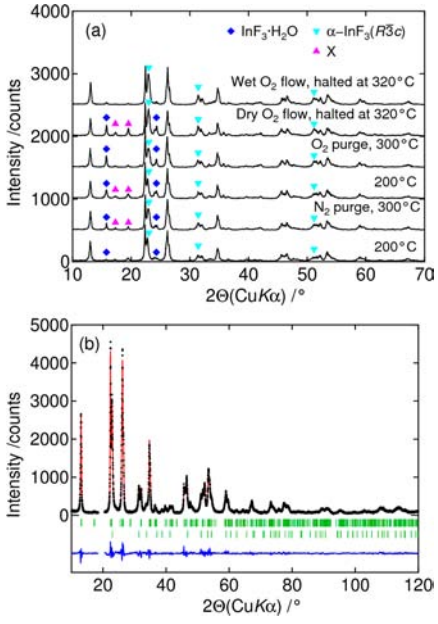

Figure 2. (a) XRD patterns of powdered samples prepared by pyrolysis of 0.5 g of $InF_3{\cdot}3H_2O$ at 200 °C or 300 °C with dry N_2 or O_2 purging prior to heating, and those obtained at 320 °C with a flow of dry or wet O_2 at 100 mL min^{-1} without retention at the target temperature. Diffraction peaks from β-InF_3 are not marked. (b) Rietveld analysis of the sample obtained at 320 °C with a wet O_2 flow.

Figure 3 shows XRD patterns of α-InF_3 formed under various atmospheres, and Table 3 lists the lattice parameters evaluated from the Rietveld analyses of these patterns. The lattice parameters of α-InF_3 in the samples synthesized with dry N_2 or O_2 flow were relatively close to those of the normal values for α-InF_3. In contrast, the lattice parameters of α-InF_3 in other samples were significantly different from the normal values, and the largest deviations were observed for α-InF_3 treated in wet atmospheres. Furthermore, the deviations were larger for α-InF_3 treated in O_2 than those treated in N_2.

Table 3 also lists the mass fractions of crystalline phases observed in the samples. Crystalline phases mainly observed after pyrolysis in wet atmospheres at 340 °C were α-InF_3 and β-InF_3. At higher temperatures and in less humid atmospheres, β-InF_3 was mostly decomposed. In contrast, α-InF_3 was more stable and detectable even in samples prepared at 420 °C.

Optical and Electrical Properties of InOF. Figure 4 shows IR absorption spectra of single-phase InOF powder shown in Figure 1d measured using the KBr pellet method. Absorption bands observed at ~3400 cm^{-1} (O−H stretching mode) and ~1650 cm^{-1} (H−O−H bending mode of H_2O) were similar to those of liquid H_2O.[11] A vacuum drying of the pellet for 3 h at 180 °C decreased the intensity of these peaks. These observations suggest that a large part of the IR absorption originates from H_2O molecules adsorbed on the surface of InOF powder. The pyrolysis in a wet atmosphere is probably the major source of the adsorbed H_2O molecules. The shoulder at ~3200 cm^{-1}, which became observable after the vacuum drying, is attributable to OH groups, most likely InOH groups at the surfaces. The amount of OH-related species, estimated on the assumption that the integrated molar absorption coefficient is equal to that of liquid H_2O and expressed as the H_2O to InOF molar ratio, was ~0.11 and ~0.05 for before and after the vacuum drying, respectively.

Single-phase InOF powder shown in Figure 1d was used to prepare InOF pellets. In N_2 or O_2, single-phase InOF pellets were obtained by sintering the powder at 360 °C. In H_2, single-phase InOF pellets were prepared at 320 °C, because In_2O_3 was formed at higher temperatures. However, the sintering of InOF powder containing a small amount (~5 at. % In) of α-InF_3 at 360 °C in H_2 or N_2 yielded single-phase InOF pellets. Such fluorine-excess precursor powder can be prepared by an incomplete oxidation, e.g., pyrolysis of $InF_3{\cdot}3H_2O$ at ~420 °C with flowing dry N_2 or O_2 (Figure 3). The relative density of these pellets was low (~50−60%), because of the low sintering temperature.

Figure 5 shows diffuse reflectance spectra recorded with single-phase InOF precursor powder and crushed pellets derived by sintering the precursor powder in N_2, O_2, or H_2. The spectrum for crushed Sn-added pellet is also shown. The spectra are plotted in Kubelka−Munk units $\alpha/S = (1 - R)^2/(2R)$, where α is the absorption coefficient, S is the scattering factor, and R is the observed reflectance. The $(\alpha h\nu/S)^2$ vs $h\nu$ plot of the precursor powder is shown in the inset. For comparison, the diffuse reflectance spectrum and $(\alpha h\nu/S)^{2/3}$ vs $h\nu$ plot of powdered In_2O_3, which is considered to be a direct

dx.doi.org/10.1021/ja405889m | J. Am. Chem. Soc. 2013, 135, 13080−13088

Table 2. Results of Rietveld Analysis of XRD Pattern Shown in Figure 2b[a]

atom	site	occup.	x	y	z	U (Å^2)
Phase 1:[b] β-InF_3·0.33H_2O, 68.0 wt %						
In	4b	1	0	1/2	0	0.0079(19)
In	8d	1	1/4	1/4	0	0.0079(19)
F	8f	1	0	0.173(12)	0.568(2)	0.032(11)
F	16h	1	0.319(14)	0.0967(8)	0.957(16)	0.032(11)
F	4c	1	0	0.537(18)	1/4	0.032(11)
F	8g	1	0.199(3)	0.219(12)	1/4	0.032(11)
O	4c	1	0	−0.032(2)	1/4	0.09(13)
Phase 2:[c] α-InF_3, 32.0 wt %						
In	6b	1	0	0	0	0.0079(19)
F	18e	1	0.626(17)	0	1/4	0.032(11)

[a]R-values: R_{wp} = 9.16%, S = 1.34. Phase 1: R_I = 1.71%, R_F = 0.82%. Phase 2: R_I = 1.30%, R_F = 0.81%. [b]Space group $Cmcm$ (no. 63), Z = 12. Lattice parameters: a = 7.890(5) Å, b = 13.467(9) Å, c = 7.943(5) Å. [c]Space group $R\bar{3}c$ (no. 167), Z = 6. Lattice parameters: a = 5.297(5) Å, c = 14.53(10) Å.

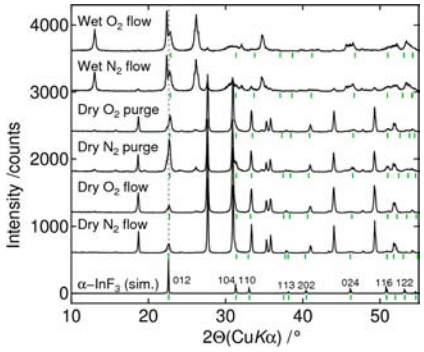

Figure 3. XRD patterns of samples obtained under various conditions. Small green bars indicate the positions of diffractions from α-InF_3 in each pattern, evaluated by Rietveld analyses. Simulated pattern of "normal" α-InF_3 (ref 9) is also shown, and the position of the 012 diffraction is denoted by a dotted line. The target temperature was 420 °C for the experiments with dry O_2 or N_2 flow, and 340 °C for other experiments. The gas flow rate for the N_2 or O_2 flow experiments was 100 mL min^{-1}.

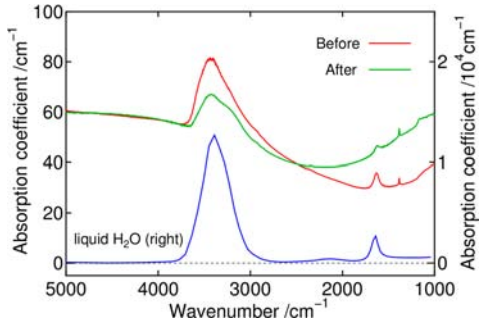

Figure 4. IR absorption spectra of single-phase InOF powder dispersed in a KBr pellet, measured before and after vacuum drying for 3 h at 180 °C. Absorption spectrum of liquid H_2O, taken from ref 11, is also shown.

forbidden band gap material,[12,13] are also shown. The band gap energy (E_g) of In_2O_3 evaluated from the inset of Figure 5 was ~2.7 eV, showing relatively good agreement with the values reported in the literature (2.9−3.0 eV).[12,13] In contrast, InOF is most likely a direct band gap material with an E_g of ~3.7 eV. The E_g value was not dependent on the atmosphere used for the sintering. However, optical absorption bands, probably attributed to lattice defects in InOF, were observed in crushed pellets from infrared to UV spectral range. The infrared absorption in the sample sintered in H_2 and the Sn-added sample was much stronger than that in the samples sintered in N_2 or O_2.

Figure 6a,b shows the electrical transport properties of InOF pellets sintered in O_2, N_2, or H_2 and Sn-added InOF pellet. At room temperature, the conductivities of the samples sintered in O_2 and N_2 were ~8.7 × 10^{-8} and ~2.1 × 10^{-7} S cm^{-1}, respectively. The conductivity of the Sn-added sample was low; it was ~1.5 × 10^{-7} S cm^{-1} and was comparable to those of the samples sintered in O_2 or N_2. Addition of α-InF_3 in the precursor powder decreased the electrical conductivity of samples sintered in N_2 (~2.1 × 10^{-8} S cm^{-1}). In contrast, sintering in H_2 distinctively increased the conductivity. The Hall coefficient was negative, indicating that electrons are the charge carriers. The highest conductivity (~2.2 S cm^{-1} at room temperature) was recorded for the sample prepared from InOF

Table 3. Lattice Parameters of α-InF_3 and Mass Fractions of Crystalline Phases Observed in Samples Shown in Figure 3[a]

	lattice parameters (Å)			mass fractions		
sample	a	c	cell volume (Å^3)	α-InF_3	β-InF_3	InOF
ref 9	5.4103(7)	14.3775(2)	364.47(7)			
dry N_2 flow, 420 °C	5.433(7)	14.30(15)	365.6(8)	0.090	0.013	0.897
dry O_2 flow, 420 °C	5.388(9)	14.37(18)	361.2(9)	0.048	0.019	0.933
dry N_2 purge, 340 °C	5.367(4)	14.403(9)	359.3(5)	0.269	0.059	0.672
dry O_2 purge, 340 °C	5.351(5)	14.451(9)	358.3(5)	0.152	0.040	0.808
wet N_2 flow, 340 °C	5.318(8)	14.54(16)	356.0(8)	0.243	0.544	0.213
wet O_2 flow, 340 °C	5.303(8)	14.54(17)	354.1(9)	0.256	0.673	0.071

[a]Minor phases other than α-InF_3, β-InF_3, and InOF were neglected for the calculation of the mass fractions.

dx.doi.org/10.1021/ja405889m | J. Am. Chem. Soc. 2013, 135, 13080−13088

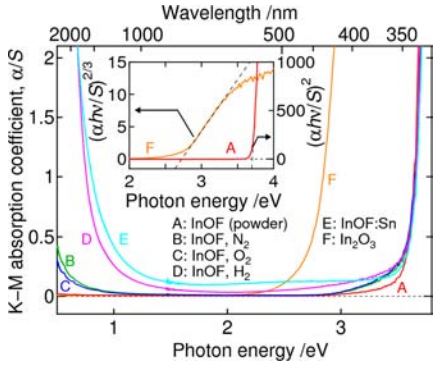

Figure 5. Diffuse reflectance spectra plotted in Kubelka–Munk (K-M) units, α/S. Spectra recorded with single-phase InOF powder, crushed InOF pellets prepared by sintering the powder in N_2, O_2, or H_2, and crushed Sn-added InOF pellet sintered in N_2, are shown. The inset shows the $(\alpha h\nu/S)^2$ vs $h\nu$ plot for the single-phase InOF powder and $(\alpha h\nu/S)^{2/3}$ vs $h\nu$ plot for In_2O_3 powder.

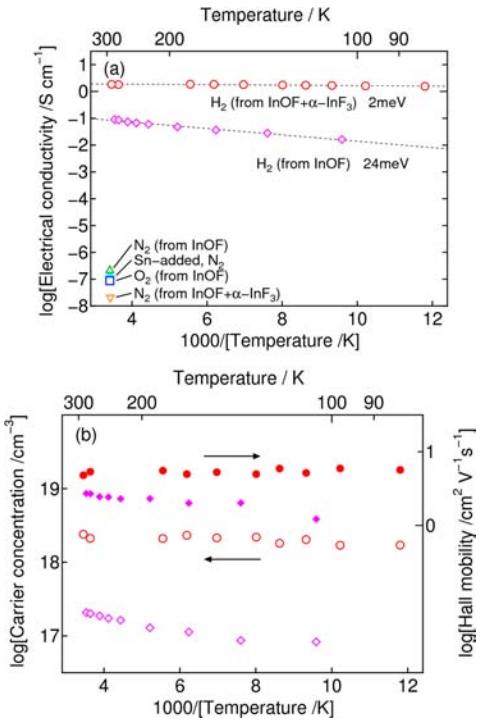

Figure 6. (a) Arrhenius plot of electrical conductivities of InOF pellets sintered in N_2, O_2, or H_2, and an Sn-added InOF pellet sintered in N_2. The InOF pellets were prepared both from single-phase InOF powder and from InOF powder containing α-InF_3. (b) Arrhenius plot of carrier concentrations and Hall mobilities of InOF pellets obtained by H_2 sintering of single-phase InOF powder (pink diamonds) and InOF powder containing α-InF_3 (red circles).

powder containing α-InF_3. The conductivity of this sample was nearly constant at or below room temperature, and the activation energy was ~2 meV. The carrier concentration and Hall mobility of the sample were $\sim 2 \times 10^{18}$ cm^{-3} and ~5 cm^2 V^{-1} s^{-1}, respectively, and were also independent of temperature. The conductivity of the sample prepared by sintering single-phase InOF powder in H_2 was smaller by ~1 order of magnitude at room temperature, and the activation energy was larger (~24 meV). This smaller conductivity was attributed mainly to the smaller carrier concentration ($\sim 2 \times 10^{17}$ cm^{-3}) in the sample.

Figure 7 shows the calculated energy band structures of InOF and In_2O_3. The conduction-band minimum (CBM) and valence-band maximum (VBM) are both located at the Γ point, indicating that InOF is a direct band gap material. The calculated E_g values are ~1.60 eV for InOF and ~1.17 eV for In_2O_3, and the ratio of these values (~1.37) agrees well with the ratio (~1.37) determined by optical absorption measurements, shown in Figure 5. The effective masses of electrons in InOF calculated from the curvatures of the CBM state along the [100], [010], and [001] directions are ~0.49m, ~0.50m, and ~0.47m, respectively, where m is the electron rest mass, indicating a nearly isotropic dispersion of the CBM state. These values are larger than that calculated along the [100] direction of the CBM state of In_2O_3 (~0.36m). Figure 8a shows the density of states (DOS) of InOF and In_2O_3. In both compounds, the CBM states consist mainly of In 5s orbitals, and the VBM states are dominated by O 2p orbitals. The F 2p orbitals are located at a lower energy than the O 2p orbitals. Figure 8b shows the logalithmic plots of partial DOS of In s orbitals of InOF and In_2O_3, indicating that the width of the conduction band of InOF is narrower than that of In_2O_3.

Figure 9 shows XPS spectra of InOF and In_2O_3. The InOF sample used for the XPS and UPS measurements was a pellet prepared by sintering single-phase InOF powder in H_2. The In_2O_3 sample was a pellet sintered in air for 2 h at 900 °C, and the electrical conductivity and the carrier concentration ($\sim 1 \times 10^{-1}$ S cm^{-1} and $\sim 4 \times 10^{16}$ cm^{-3}, respectively) were comparable to those of the InOF sample. As shown in the inset of Figure 9a, the binding energy of the VB edge of InOF was smaller by ~0.9 eV than that of In_2O_3. The peak position of the In $3d_{5/2}$ levels of In_2O_3 (~444.7 eV), shown in Figure 9b, agreed well with the literature values (444.5–445.2 eV[14–16]). The In $3d_{5/2}$ level was at ~445.6 eV in InOF. The peak separation (~0.9 eV) was nearly half that of the separation of the In $3d_{5/2}$ levels between In_2O_3 and InF_3 (~1.5 eV[14]). Similar peak shifts were observed for all peaks of the In 4d, In 3d, and In 3p levels. The O 1s level of In_2O_3, shown in Figure 9c, consisted of a peak at ~530.2 eV and a shoulder at the higher energy side, attributable to bulk O^{2-} ions and O^{2-} ions associated with defect sites or OH groups, respectively.[15,17] The O 1s level of InOF also consisted of a peak at ~531.0 eV and a shoulder at the higher energy side. This shoulder probably originates from surface OH-related species associated with fluorine.[18,19] The O 2s levels of these compounds, which are expected to be located at ~20 eV, could not be resolved, probably because of interference from the intense In 4d peaks. Figure 9d shows spectra around F 1s peak. The peak position of F 1s peak in InOF was ~685.3 eV.

Figure 10 shows the results of the UPS measurements. The signals arising from the electrons at the Fermi level were undetectable, because of the low carrier concentrations in these samples. The VBM energy with respect to the secondary electron cutoff (E_{VBM}) was ~14.0 eV for InOF and ~13.3 eV for In_2O_3. The separation between the vacuum level and VBM, defined by $h\nu$(He I) − E_{VBM}, was ~7.2 eV for InOF and ~7.9 eV for In_2O_3. Figure 11 shows a schematic energy-level diagram of InOF and In_2O_3 drawn using these data. The CBM positions were determined using the E_g values evaluated in Figure 5.

■ DISCUSSION

The overall reaction of the formation of InOF by pyrolysis of $InF_3 \cdot 3H_2O$ may be described as

dx.doi.org/10.1021/ja405889m | J. Am. Chem. Soc. 2013, 135, 13080–13088

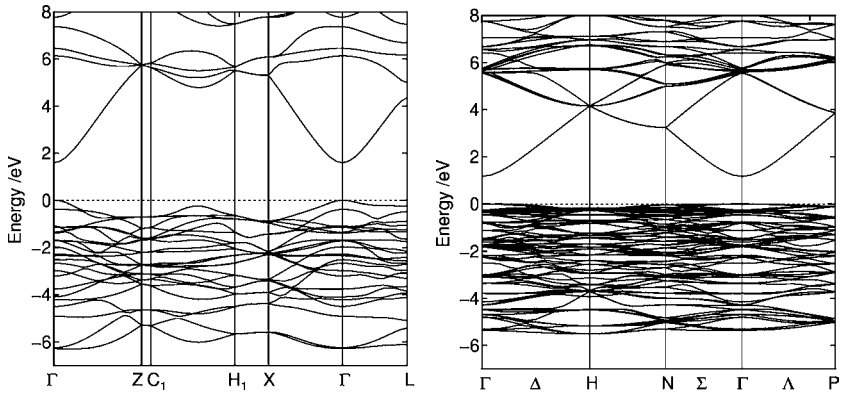

Figure 7. Calculated band structures of (left) InOF and (right) In_2O_3. Symbols on the abscissa denote special k points in the reciprocal space of a face-centered tetragonal lattice for InOF and a body-centered cubic lattice for In_2O_3. Their coordinates in the Brillouin zone with respect to the reciprocal conventional vectors are (0, 0, 0) for Γ, (0, 0, 1) for Z, (0.1319, 0, 1) for C_1, (1, 0, 0.3840) for H_1, (1, 0, 0) for X, (1/2, 1/2, 1/2) for L, (1, 0, 0) for H, (1/2, 1/2, 0) for N, and (1/2, 1/2, 1/2) for P.

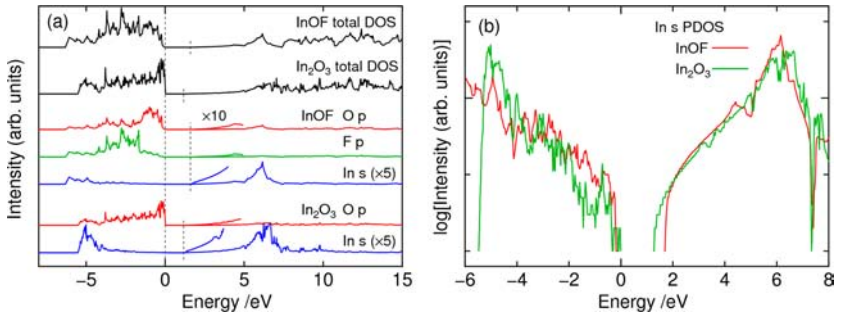

Figure 8. (a) Calculated total and partial density of states of InOF and In_2O_3. Energies are measured from VBM, and the positions of CBM are denoted by dotted lines. Spectra obtained by magnifying the displayed plots 10 times (actual magnifications for In s plots are ×50) are also shown near CBM. (b) Logarithmic plots of partial density of states of In s orbitals in InOF and In_2O_3.

$$InF_3{\cdot}3H_2O \rightarrow InOF + 3/2H_2O + 3HF \quad (1)$$

This reaction generates water as a byproduct. However, InOF is reported to be unstable in a wet atmosphere above 320 °C.[4] Indeed, InOF obtained in this study was rapidly decomposed in water. Such instability of InOF toward water makes it difficult to synthesize InOF using this process.

Figures 1a,b shows the results of the pyrolysis of $InF_3{\cdot}3H_2O$ without a gas flow, where the generated water vapor remains in the tube furnace. In these experiments, the decomposition of InOF by water vapor,

$$2InOF + H_2O \rightarrow In_2O_3 + 2HF \quad (2)$$

probably determines the InOF stability. This mechanism reasonably explains the observations that the lowest temperature for the formation of In_2O_3 (~460 °C) is independent of the type of purged gas (N_2 or O_2) (Figure 1a,b), whereas it increases when the humidity is lowered by continuous gas flow during the pyrolysis (Figure 1c).

The formation mechanism of InOF is more complicated. As shown in Figure 1d, the best way to obtain a large amount of single-phase InOF is to pyrolyze $InF_3{\cdot}3H_2O$ with a wet O_2 flow below ~300 °C and with a dry O_2 flow above the temperature. It appears from Figure 2a that water vapor enhances decomposition of the unknown phase X and $InF_3{\cdot}3H_2O$, although the reason and mechanisms remain unclear. Phase X is probably a new hydrate of InF_3, because α-InF_3 hydrated at room temperature has been reported to give a similar XRD pattern.[20] However, it was not possible to associate this pattern (PDF 46-0214) with a single phase, and the pattern most likely contains diffraction peaks from $InF_3{\cdot}3H_2O$, which may be formed by further hydration of phase X. The details of the unknown phase Y, which appears as a minor impurity phase at this temperature range in the O_2-treated samples, remain unclear.

The main products of the wet O_2 pyrolysis of $InF_3{\cdot}3H_2O$ at ~300 °C are β-InF_3 and a variant of α-InF_3 (Figure 2b). β-InF_3 is a metastable phase, isostructural with several fluorides of trivalent cations, including β-AlF_3, β-GaF_3, and β-FeF_3.[9] "γ-InF_3" reported in ref 21 (PDF 27-1160) is probably a wrong assignment of β-InF_3. This structure is similar to the hexagonal tungsten−bronze structure and has one-dimensional channels along the c-axis. The channels in β-FeF_3 incorporate H_2O molecules up to the composition β-$FeF_3{\cdot}0.33H_2O$. However, the atomic positions of β-InF_3 have not yet been reported. Table 2 lists the structural parameters tentatively determined from the Rietveld analysis shown in Figure 2b; the data suggest the presence of H_2O in the channels of β-InF_3. The fit is worse in the H_2O-free model. These observations imply that H_2O molecules act as templates for the formation of metastable hydrated β-InF_3. Figure 3 and Table 3 suggest that β-InF_3 becomes unstable at higher temperatures and in less humid atmospheres and is decomposed into α-InF_3 and InOF.

The data in Table 3 show that the lattice parameters of α-InF_3 change continuously with the changing atmosphere during the pyrolysis, suggesting a tendency of α-InF_3 to form solid solutions or nonstoichiometric phases. Anion vacancies can be formed by simple fluorine loss (α-InF_{3-x}) or anion exchange between F^- and O^{2-} ions (α-$InF_{3-2x}O_x$). The anion vacancies

dx.doi.org/10.1021/ja405889m | J. Am. Chem. Soc. 2013, 135, 13080−13088

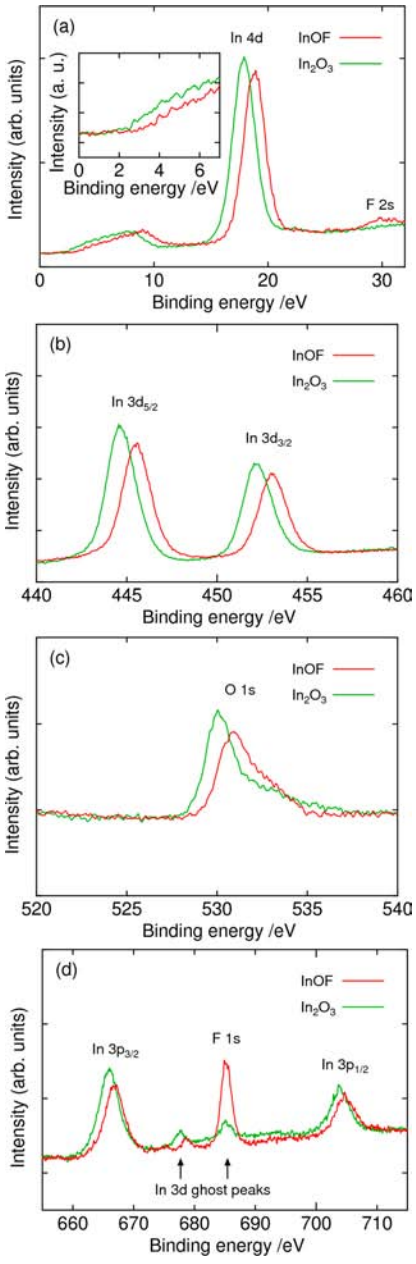

Figure 9. XPS spectra of InOF and In_2O_3: (a) around the valence-band edge, (b) In 3d levels, (c) O 1s level, and (d) In 3p and F 1s levels. Arrows in panel d indicate In 3d ghost peaks induced by excitation with Mg $K\alpha$ line ($h\nu$ = 1253.6 eV).

usually create midgap states, which induce additional absorption bands within the band gap. However, the samples listed in Table 3 are colorless, despite the large variations in the lattice parameters. Furthermore, the lattice parameters of α-InF_3 in the sample treated under a dry O_2 flow are relatively close to the normal values. The observed changes in the lattice parameters are therefore unlikely to result from anion vacancies. The variations in the lattice parameters are larger for the purge experiments than for the dry-gas-flow experiments, and the variations are largest for the samples formed under the most water-rich conditions (wet O_2 or N_2 flow). From these observations, we suggest that the changes in the lattice parameters of α-InF_3 are the result of the formation of hydrated forms of α-InF_3, namely, α-$InF_{3-x}(OH)_x$. The greater changes in the lattice parameters in O_2 than in N_2 imply the

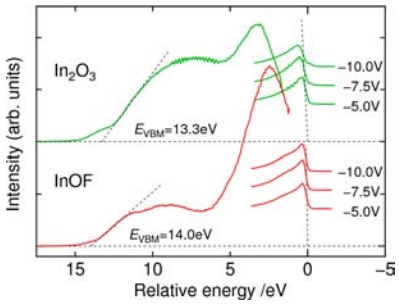

Figure 10. UPS spectra of InOF and In_2O_3 plotted with respect to the secondary electron cutoff. The spectra near the valence-band edge were measured without applying a bias voltage. The spectra for the secondary electron peaks are corrected for bias voltages.

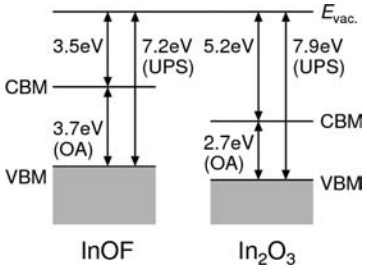

Figure 11. Schematic energy-level diagram of InOF and In_2O_3, determined from the optical absorption measurements shown in Figure 5 and UPS measurements shown in Figure 10.

presence of cooperative effects between H_2O and O_2, e.g., an enhancement of uptake of OH groups by an acceleration of fluorine loss in O_2.

Both of the hydrated forms of α-InF_3 and β-InF_3 are considered to be direct precursors of InOF, and the conversion reaction proceeds above ~340 °C. Water molecules and OH groups in these fluorides probably act as oxygen sources to facilitate the formation of InOF. The conversion is easier in O_2 than in N_2 (Figures 1a,b), indicating the participation of ambient O_2 in the oxidation of the fluorides to InOF in an O_2 atmosphere.

Recently, cation−anion bond ionicity of oxyfluorides including $K_3WO_3F_3$,[22] $CsMnMoO_3F_3$,[23] and Rb_2KTiOF_5[24] has been evaluated by XPS. The binding energy (BE) difference of core levels of constituent elements has been taken as the parameter related to the bond ionicity, where the lower BE difference indicates higher ionicity. BE(O 1s) − BE(In $3d_{5/2}$) evaluated from Figure 9 is ~85.4 eV for InOF and ~85.5 eV for In_2O_3. Thus, the ionicity of In−O bonds in InOF is slightly higher than those in In_2O_3. BE(F 1s)−BE(In $3d_{5/2}$) of InOF evaluated from Figure 9 is ~239.7 eV. This value is most likely located at ~239 eV for InF_3,[25] suggesting a lower ionicity of In−F bonds in InOF than those in InF_3. These ionicity variation trends are the same as that in the complex oxyfluorides mentioned above.[22−24]

Figure 6a shows that sintering in an H_2 atmosphere distinctively increases the electrical conductivity of InOF. We suggest that the conduction electrons originate from fluorine vacancies, because a strong H_2 reduction forms In_2O_3. The preferential loss of fluorine results from the smaller coordination number of fluorine (2) than that of oxygen (4). α-InF_3 remaining in the precursor powder does not participate in the carrier generation by the substitution of fluorine into oxygen sites of InOF because it decreases the electrical

dx.doi.org/10.1021/ja405889m | J. Am. Chem. Soc. 2013, 135, 13080−13088

conductivity of samples sintered in N_2 (Figure 6a). Thus, the anion substitution is not easy, and the probable role of α-InF_3 is to suppresses inhomogeneous oxidation from the particle surfaces and to form fluorine vacancies uniformly over samples at higher concentrations. However, the carrier concentrations of these samples ($\sim 10^{17}-10^{18}$ cm^{-3}) are much smaller than the concentration of anion sites in InOF, suggesting that the stability of InOF is low against the formation of fluorine vacancies. These interpretations are consistent with the observations that the lattice parameters of InOF are not influenced by the sintering atmosphere and the incorporation of α-InF_3 in the precursor powder.

Figure 6 shows that sintering in H_2 yields InOF samples with nearly degenerate electrical conduction, although the carrier concentration is as small as $\sim 10^{18}$ cm^{-3}. Thus, the donor level of the sample is expected to be very shallow. Similar degenerate electrical conduction is also reported for single-crystalline In_2O_3[26] and $InGaO_3(ZnO)_5$[27] films at carrier concentrations larger than $\sim 10^{18}$ cm^{-3}. It is probably because of the large effective Bohr radius of electrons in indium- and zinc-based ceramics (~20–50 Å for In_2O_3[26]).

The effective masses of electrons in InOF and In_2O_3 calculated from Figure 7 ($\sim 0.47-0.50m$ and $\sim 0.36m$, respectively) suggest that the mobility of electrons in InOF is somewhat smaller than that in In_2O_3. This difference may result from the fewer close In neighbors in InOF. Figure 12 shows the

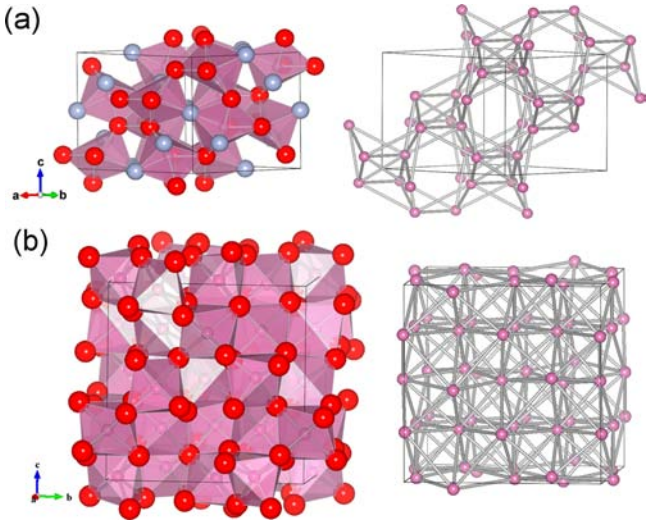

Figure 12. Crystal structures of (a) InOF and (b) In_2O_3 (space group no. 206, $Ia\bar{3}$) drawn with VESTA.[36] Red, gray, and pink spheres denote O, F, and In atoms, respectively. The InO_4F_2 octahedra in InOF and the InO_6 octahedra in In_2O_3 are highlighted. The right panels show the distributions of In atoms and the In–In distances shorter than 4 Å.

crystal structures of InOF and In_2O_3, and the In–In distances shorter than 4 Å. The radial distributions of In atoms around each In site in InOF and In_2O_3 are shown in Figure 13. The number of the In–In distances shorter than 4 Å is 9 for InOF and 12 for In_2O_3, and the number of the shortest In–In bonds in InOF (3) is smaller than that in In_2O_3 (6).

The number of close In neighbors is fewer in InOF, because the number of In atoms around an F atom (2) is fewer than that around an O atom (4), both in InOF and In_2O_3. As a consequence, one-dimensional cavities are formed in the In–In network through the positions of F atoms, along the [110] and

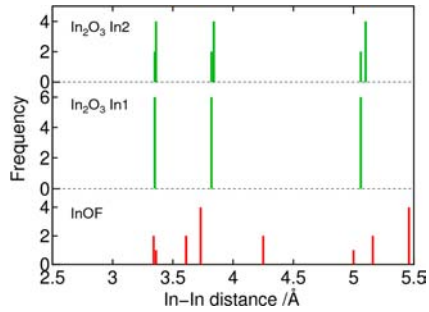

Figure 13. Radial distributions of In atoms around each In site in InOF and In_2O_3. For In_2O_3, In atoms located at the 8b and 24d sites are denoted by In1 and In2, respectively.

[$1\bar{1}0$] directions of InOF (Figure 12). Because of the cavity presence, the In–In network in InOF is uneven. However, this uneven In–In network makes it possible to maintain a good connectivity between the In atoms, while compensating for the smaller concentration of In atoms in InOF (2.67×10^{22} cm^{-3}) compared with that in In_2O_3 (3.09×10^{22} cm^{-3}). Indeed, the shortest In–In distances (~3.35 Å) are nearly the same in these compounds.

The Hall mobility of electrons in In_2O_3 is ~100–200 cm^2 V^{-1} s^{-1} for single crystals,[26,28,29] ~10–40 cm^2 V^{-1} s^{-1} for polycrystalline samples,[30,31] and ~14 cm^2 V^{-1} s^{-1} for the polycrystalline In_2O_3 pellet prepared in this study (relative density, ~64%). Thus, the intrinsic electron mobility in InOF would be much larger than the value observed in this study (~5 cm^2 V^{-1} s^{-1}). The small mobility is attributable to the polycrystalline nature and the small relative density (~50–60%).

Figure 6 indicates that the donor level of the InOF samples sintered in H_2 is very shallow, and thus the Fermi level of this sample is almost identical to the CBM energy. The Fermi level of the In_2O_3 sample is also expected to be located closely to CBM. The work function of In_2O_3 evaluated on the bases of the assumptions and Figure 11 is ~5.2 eV and is consistent with the literature values.[32,33] The work function of InOF derived in a similar manner is ~3.5 eV, smaller by ~1.5 eV than that of In_2O_3. Such a decrease in the work function as a result of fluorination is opposite to the changes observed in indium tin oxide (ITO) films subjected to plasma treatments with fluorinated gases.[25,34] A recent report shows that surface chlorination also increases the work function of ITO; this is attributable to the formation of surface In–Cl bonds, which induce dipoles across the surface and change the electrostatic potential just outside the surface.[35] In contrast, the small work function of InOF compared with that of In_2O_3 should be a bulk phenomenon, implying different roles of fluorine in the bulk and at the surface of indium-based oxides.

The small work function of InOF is explained by the fewer close In neighbors in InOF. It probably narrows the conduction band, which consists mainly of In 5s orbitals (Figure 8b) and shifts the CBM upward. The control of the topology of the conduction path, typically shown in Figure 12, can be an interesting approach in modifying the electronic structure of transparent conductive ceramics.

■ CONCLUSIONS

We developed a reliable procedure for the synthesis of single-phase InOF powder under ambient pressure, by controlling the atmosphere and moisture during pyrolysis of $InF_3 \cdot 3H_2O$. The

dx.doi.org/10.1021/ja405889m | J. Am. Chem. Soc. 2013, 135, 13080–13088

main intermediate phases generated during the pyrolysis are hydrated forms of α- and β-InF_3, and their self-decomposition as well as additional oxidation with ambient oxygen and water molecules play a key role in the formation of InOF. Observations indicate that InOF is an ultraviolet-transparent direct band gap material with a band gap energy of ∼3.7 eV. In comparison with In_2O_3, the conductivity of InOF pellets can be controlled more widely, over ∼8 orders of magnitude, by changing the sintering atmosphere. Sintering in H_2 yields samples with nearly degenerate n-type conductivity of ∼2 S cm^{-1}. However, neither Sn nor excess fluorine incorporations are effective in increasing the electrical conductivity. The energy of the conduction band minimum with respect to the vacuum level is higher by ∼1.5 eV in InOF than in In_2O_3, resulting in a strikingly small work function of InOF (∼3.5 eV) as compared with that of In_2O_3 (∼5 eV).

AUTHOR INFORMATION

Corresponding Author

kkaji@tmu.ac.jp

Notes

The authors declare no competing financial interest.

ACKNOWLEDGMENTS

K.K. thanks Mr. Ryo Harada and Dr. Yasuhiro Akita of Tokyo Metropolitan University for assistance in the IR absorption measurements. Study at Tokyo Institute of Technology was supported by the Collaborative Research Project of Materials and Structures Laboratory, Tokyo Institute of Technology, and MEXT Elements Strategy Initiative to Form Core Research Center.

REFERENCES

(1) Shigesato, Y.; Shin, N.; Kamei, M.; Song, P. K.; Yasui, I. *Jpn. J. Appl. Phys.* **2000**, *39*, 6422.

(2) Goggin, P. L.; McColm, I. J.; Shore, R. *J. Chem. Soc. A* **1966**, 1004.

(3) Mermant, G.; Belinski, C.; Lalan-Keraky, F. *C. R. Seances Acad. Sci., Ser. C* **1966**, *263*, 1216.

(4) Chamberland, B. L.; Babcock, K. R. *Mater. Res. Bull.* **1967**, *2*, 481.

(5) Vlasse, P. M.; Massies, J. C.; Chamberland, B. L. *Acta Crystallogr., Sect. B: Struct. Crystallogr. Cryst. Chem.* **1973**, *29*, 627.

(6) Izumi, F.; Momma, K. *Solid State Phenom.* **2007**, *130*, 15.

(7) Blaha, P.; Schwarz, K.; Madsen, G. K. H.; Kvasnicka, D.; Luitz, J. *WIEN2k, An Agumented Plane Wave + Local Orbitals for Calculating Crystal Properties*; Schwarz, K., Ed.; Techn. Universitat: Wien, Austria, 2001.

(8) Hoppe, R.; Kissel, D. *J. Fluorine Chem.* **1984**, *24*, 327.

(9) Le Bail, A.; Jacoboni, C.; Leblanc, M.; De Pape, R.; Duroy, H.; Fourquet, J. L. *J. Solid State Chem.* **1988**, *77*, 96.

(10) Bukovec, P.; Kaučič, V. *Inorg. Nucl. Chem. Lett.* **1978**, *14*, 79.

(11) Hale, G. M.; Querry, M. R. *Appl. Opt.* **1973**, *12*, 555.

(12) Walsh, A.; Silva, J. L. F. D; Wei, S.; Körber, C.; Klein, A.; Piper, L. F. J.; DeMasi, A.; Smith, K. E.; Panaccione, G.; Torelli, P.; Payne, D. J.; Bourlange, A.; Egdell, R. G. *Phys. Rev. Lett.* **2008**, *100*, 167402.

(13) King, P. D. C.; Veal, T. D.; Fuchs, F.; Wang, Ch. Y.; Payne, D. J.; Bourlange, A.; Zhang, H.; Bell, G. R.; Cimalla, V.; Ambacher, O.; Egdell, R. G.; Bechstedt, F.; McConville, C. F. *Phys. Rev. B* **2009**, *79*, 205211.

(14) McGuire, G. E.; Schweitzer, G. K.; Carlson, T. A. *Inorg. Chem.* **1973**, *12*, 2450.

(15) Fan, J. C. C.; Goodenough, J. B. *J. Appl. Phys.* **1977**, *48*, 3524.

(16) Hewitt, R. W.; Winograd, N. *J. Appl. Phys.* **1980**, *51*, 2620.

(17) Han, S.-Y.; Herman, G. S.; Chang, C.-H. *J. Am. Chem. Soc.* **2011**, *133*, 5166.

(18) Wuttke, S.; Coman, S. M.; Scholz, G.; Kirmse, H.; Vimont, A.; Daturi, M.; Schroeder, S. L. M.; Kemnitz, E. *Chem.—Eur. J.* **2008**, *14*, 11488.

(19) Makarowicz, A.; Bailey, C. L.; Weiher, N.; Kemnitz, E.; Schroeder, S. L. M.; Mukhopadhyay, S.; Wander, A.; Searlec, B. G; Harrison, N. M. *Phys. Chem. Chem. Phys.* **2009**, *11*, 5664.

(20) Fedorov, P. P.; Zibrov, I. P.; Sobolev, B. P.; Shishkin, I. V.; Fedorov, P. I.; Sviderskii, M. F.; Petranin, N. P. *Russ. J. Inorg. Chem.* **1989**, *34*, 412.

(21) Beck, L. K.; Kugler, B. H.; Haendler, H. M. *J. Solid State Chem.* **1973**, *8*, 312.

(22) Atuchin, V. V.; Gavrilova, T. A.; Kesler, V. G.; Molokeev, M. S.; Aleksandrov, K. S. *Solid State Commun.* **2010**, *150*, 2085.

(23) Atuchin, V. V.; Molokeev, M. S.; Yurkin, G. Y.; Gavrilova, T. A.; Kesler, V. G.; Laptash, N. M.; Flerov, I. N.; Patrin, G. S. *J. Phys. Chem. C* **2012**, *116*, 10162.

(24) Atuchin, V. V.; Isaenko, L. I.; Kesler, V. G.; Kang, L.; Lin, Z.; Molokeev, M. S.; Yelisseyev, A. P.; Zhurkov, S. A. *Phys. Chem. C* **2013**, *117*, 7269.

(25) Ikagawa, M.; Tohno, I.; Shinmura, T.; Takagi, S.; Kataoka, Y.; Fujihira, M. *Jpn. J. Appl. Phys.* **2008**, *47*, 8935.

(26) Bierwagen, O.; Speck, J. S. *Appl. Phys. Lett.* **2010**, *97*, 072103.

(27) Nomura, K.; Kamiya, T.; Ohta, H.; Ueda, K.; Hirano, H.; Hosono, H. *Appl. Phys. Lett.* **2004**, *85*, 1993.

(28) Weiher, R. L. *J. Appl. Phys.* **1962**, *33*, 2834.

(29) Koida, T.; Kondo, M. J. *Appl. Phys.* **2006**, *99*, 123703.

(30) de Wit, J. H. W.; van Unen, G.; Lahey, M. *J. Phys. Chem. Solids* **1977**, *58*, 819.

(31) Ambrosini, A.; Palmer, G. B.; Maignan, A.; Poeppelmeier, K. R.; Lane, M. A.; Brazis, P.; Kannewurf, C. R.; Hogan, T.; Mason, T. O. *Chem. Mater.* **2002**, *14*, 52.

(32) Sato, Y.; Tokumaru, R.; Nishimura, E.; Song, P.-K.; Shigesato, Y.; Utsumi, K.; Iigusa, H. *J. Vac. Sci. Technol., A* **2005**, *23*, 1167.

(33) Klein, A.; Körber, C.; Wachau, A.; Säuberlich, F.; Gassenbauer, Y.; Schafranek, R.; Harvey, S. P.; Mason, T. O. *Thin Solid Films* **2009**, *518*, 1197.

(34) Choi, B.; Yoon, H.; Lee, H. H. *Appl. Phys. Lett.* **2000**, *76*, 412.

(35) Helander, M. G.; Wang, Z. B.; Qiu, J.; Greiner, M. T.; Puzzo, D. P.; Liu, Z. W.; Lu, Z. H. *Science* **2011**, *332*, 944.

(36) Momma, K.; Izumi, F. *J. Appl. Crystallogr.* **2011**, *44*, 1272.